Alternate Splicing Directs PMCA2 to Lysosomes and is Linked to Neurodegeneration

Fernández-Suárez, M.E.[1,2], Bush, R.[1,3], Brenton, J.W.[2,4,5,6,7], Pereira, G.[8,9], Grant-Peters, M.[7,10], Reynolds, R.[5,6], te Vruchte, D.[1,2], Shepherd, D.[1], Weng, Y.[1], Artaza-Fernández, E.[1], Lis, P.[2,11], Sanchez-Pulido, L.[12], Morgan, A.[1], Davis, L.[1], Gómez-Coronado, D.[13], Eden, E.[14], Alessi, D.[2,11], Ponting, C.P.[12], Galione, A [1], Newstead, S.[3,15], Hardy, J.[2,16,17], Patel, S.[8], Ryten, M.[2,7,10,18], and Platt, F.M[*1,2].

1. Department of Pharmacology, University of Oxford, Oxford, UK.

2. Aligning Science Across Parkinson's (ASAP) Collaborative Research Network, Chevy Chase, MD, USA.

3. Department of Biochemistry, University of Oxford, Oxford, UK.

4. UCL Queen Square Institute of Neurology, Department of Neurodegenerative Diseases, London, UK.

5. Department of Genetics and Genomic Medicine, Great Ormond Street Institute of Child Health, University College London, London, UK.

6. NIHR Great Ormond Street Hospital Biomedical Research Centre, University College London, London, UK.

7. UK Dementia Research Institute at The University of Cambridge, Cambridge, UK.

8. Department of Cell and Developmental Biology, University College London, London, UK.

9. Department of Pharmacology, Federal University of São Paulo (UNIFESP), São Paulo, Brazil.

10. Department of Clinical Neurosciences, School of Clinical Medicine, University of Cambridge, Cambridge, UK

11. Medical Research Council (MRC) Protein Phosphorylation and Ubiquitylation Unit, School of Life Sciences, University of Dundee, Dundee, UK.

26 12. MRC Human Genetics Unit, Institute of Genetics & Cancer, University of Edinburgh,
27 Edinburgh, UK.
28 13. Department of Biochemistry-Research, Hospital Universitario Ramón y Cajal, IRYCIS,
29 Madrid, Spain.
30 14. Institute of Ophthalmology, University College London, London, UK.
31 15. Kavli Institute for Nanoscience Discovery, University of Oxford, Oxford, UK.
32 16. Department of Neurodegenerative Disease, UCL Institute of Neurology, UK.
33 17. UK Dementia Research Institute at UCL, London, UK.
34 18. Department of Medical Genetics, NIHR Cambridge Biomedical Research Centre,
35 University of Cambridge, Cambridge, UK.
36 * Corresponding author: frances.platt@pharm.ox.ac.uk

Abstract

Plasma membrane calcium ATPase (PMCAs) are believed to function exclusively at the plasma membrane where they expel calcium from the cytosol. We have unexpectedly identified a splice variant-dependent localisation of the PMCA isoform PMCA2 to the lysosome, where it forms an evolutionarily conserved complex with NPC1, the lysosomal membrane protein defective in the rare lysosomal storage disease Niemann-Pick disease type C (NPC). This interaction is involved in maintaining lysosomal calcium levels, and we have found its disruption contributes to the pathophysiology of both NPC and Parkinson's disease. Our findings uncover a previously unrecognised intracellular role for PMCA2, revealing a shared mechanism of lysosomal calcium and lipid regulation with direct relevance to neurodegeneration.

Introduction

Precise regulation of intracellular calcium (Ca^{2+}) homeostasis is essential for neuronal function and survival. Plasma membrane calcium ATPases (PMCAs) are high-affinity Ca^{2+} pumps that move cytosolic Ca^{2+} across the plasma membrane to the extracellular environment [1]. Of the four PMCA isoforms in humans (PMCA1–4), PMCA2 and PMCA3 are highly expressed in neurons in the brain, with PMCA2 particularly enriched in cerebellar Purkinje cells [1]. Loss-of-function mutations in PMCA2 or PMCA3 cause progressive cerebellar ataxia [2 3 4], and reduced PMCA2 expression has been associated with increased vulnerability of dopaminergic neurons in Parkinson's disease (PD) [5]. Moreover, soluble α-synuclein, implicated in PD pathogenesis, directly enhances PMCA1/2 activity, underscoring the relevance of PMCA regulation in neurodegeneration [6]. To date, all functional roles of PMCAs have been attributed to its localisation at the plasma membrane. However, the genes encoding the PMCAs are alternatively spliced, raising the possibility that they could have additional localisations and functions.

In a yeast screen, we previously identified PMC1, the single yeast orthologue of mammalian PMCAs, as a direct interactor of Ncr1, the yeast orthologue of mammalian NPC1 [7]. This interaction was conserved in mammalian cells [7]. NPC1 is a thirteen-transmembrane lysosomal protein encoded by *NPC1* that is mutated in the rare neurodegenerative lysosomal storage disorder, Niemann-Pick disease type C (NPC). NPC1 deficiency results in disrupted lysosomal lipid homeostasis, impaired lysosome: ER membrane contact site formation and, critically, lowered levels of lysosomal luminal Ca^{2+} [8], potentially due to a Ca^{2+} store filling defect, a feature also reported in PD [9]. However, the molecular mechanism underlying Ca^{2+} import into the lysosome remains incompletely understood.

Here, we show that alternative splicing directs specific PMCA2 isoforms to the lysosome, where they form a complex with NPC1 to regulate lysosomal Ca^{2+} levels. These findings have

uncovered a conserved calcium regulatory axis with broad implications for lysosome function and neurodegenerative diseases. This study also highlights that splice variants can differentially affect subcellular organelle targeting of proteins, expanding the function of proteins beyond their canonical roles.

Results

PMCA2 colocalises with NPC1 in the lysosome.

We previously demonstrated that NPC1 and PMCA2 from rat cerebellum co-immunoprecipitate [7]. To determine whether this interaction occurs at the lysosomal membrane, we examined the localisation of endogenous PMCA2 in rat PC12 cells, a cell line reported to express PMCA2 and that can be differentiated into neurons [10 11]. Immunocytochemistry with a pan anti-PMCA2 polyclonal antibody that recognises all splice variants, followed by confocal microscopy, revealed that endogenous PMCA2 colocalised with the lysosomal protein NPC1, with no detectable signal at the plasma membrane (Fig. 1a). Individual staining controls of PMCA2 and NPC1 showed no bleed-through between channels or non-specific staining when no primary antibody was present (Supplementary Figure 1). To test the specificity of the anti-PMCA2 antibody, we knocked down (KD) the expression of endogenous PMCA2 in PC12 cells by stably expressing a shRNA targeting *Atp2b2*, the gene encoding the PMCA2 protein. Immunocytochemistry showed a distinct punctate pattern consistent with lysosomal localisation of PMCA2 in wild type (WT) cells that was absent in the *Atp2b2* KD cells (Supplementary Figure 2).

To confirm these results, we used a complementary technique isolating lysosomes from the cerebellum of WT mice using Tagless LysoIP [12]. Lysosomes were immunoprecipitated using a monoclonal antibody bound to magnetic beads that binds a cytosolic epitope of the endogenous lysosomal membrane protein TMEM192. As a negative control, magnetic beads bound to an isotype-matched control antibody were used. The purified lysosomes were analysed using western blotting probing using the anti-PMCA2 polyclonal antibody, and a band of approximately 130 kDa was detected in the input fraction (Figure 1b). This band

corresponded to the predicted molecular weight of PMCA2 and was statistically significantly enriched in the lysosomal fraction isolated from the cerebellum (Figure 1c).

Having confirmed the lysosomal localisation of PMCA2, we modelled the PMCA2 structure and orientation in the limiting membrane of the lysosome and its direct interaction with NPC1 using AlphaFold 3 software. The resulting human NPC1-PMCA2 complex (Fig. 1d) models both the N- and C-terminal domains of PMCA2 on the cytosolic face of the lysosomal membrane, an orientation compatible with Ca^{2+} import into the lysosome (red arrow, Figure 1d and e). Strikingly, a corresponding AlphaFold 3 model of the yeast Pmc1/Ncr1 complex (Fig. 1e) reveals a conserved topology, suggesting evolutionary conservation of the formation and function of this complex.

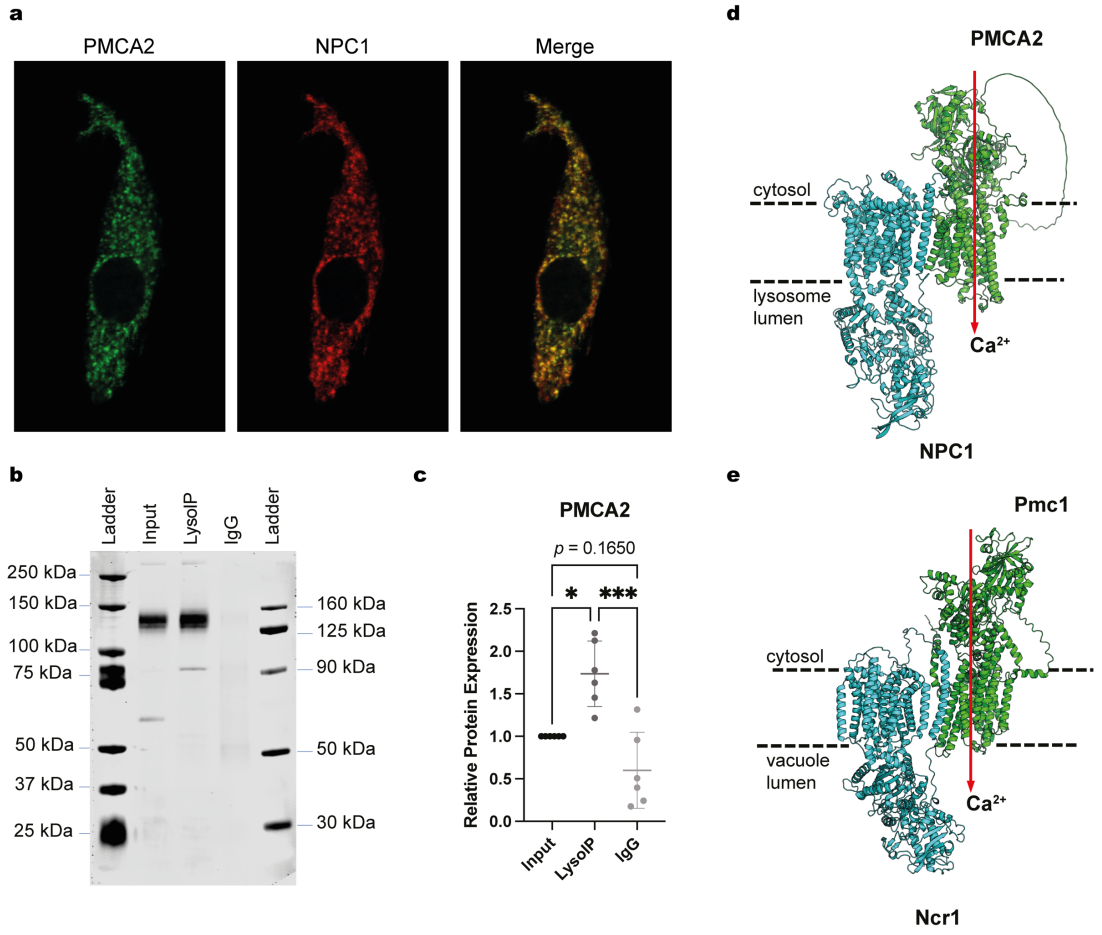

120 **Figure 1. PMCA2 is present in the lysosome.** (a) Immunocytochemistry and confocal
121 microscopy showed that endogenous PMCA2 colocalises with NPC1 in the lysosome of PC12
122 cells differentiated into neurons. NPC1 and PMCA2 were detected using primary antibodies
123 directly labelled with CoraLite-555 and CoraLite-488, respectively. Representative image of
124 five independent experiments, Pearson's coefficient r = 0.8636 ± 0.0437 standard deviation
125 corresponding to the mean of five independent experiments, calculated using the mean of r
126 from 10 fields per experiment. (b) Representative image of Tagless LysoIP followed by
127 Western blot probing for PMCA2 in mouse cerebellar tissue, $n = 6$ mice. (c) Quantification of
128 PMCA2 enrichment in lysosomal fraction from LysoIP experiments, $n = 6$ mice, lines represent
129 the mean and standard deviation, one-way Anova test, $*p < 0.05$, $***p < 0.001$. (d) AlphaFold 3
130 model of the PMCA2-NPC1 complex in the lysosomal membrane. Directionality of Ca^{2+}
131 transport is represented with a red arrow (e) AlphaFold 3 model of yeast orthologues Ncr1 and
132 Pmc1 in the vacuolar membrane exhibiting a similar orientation and interaction.
133
134 **PMCA2 depletion disrupts lysosomal Ca^{2+} signalling.**
135 The discovery of the lysosomal localisation of PMCA2 and the orientation of PMCA2 in the
136 complex with NPC1 raised the possibility that it could play a key role in filling the lysosome
137 with Ca^{2}. To test this hypothesis, we used the PC12 *Atp2b2* KD cells described above. The
138 shRNA construct used to generate these cells contained a GFP cassette as a positive control of
139 transduction. These cells were differentiated into neurons and then loaded with Fura-2, a
140 fluorescent probe that accumulates in the cytoplasm. Lysosomal Ca^{2+} levels were inferred by
141 monitoring Ca^{2+} release into the cytoplasm. In these experiments, we used PC12 cells stably
142 expressing a scramble shRNA and differentiated into neurons as controls. To specifically
143 evaluate Ca^{2+} release from the lysosome, we stimulated the cells with a synergistic combination
144 of the lysosomal TPC2 calcium channel agonists TPC2-A1N and TPC2-A1P [13] (both at 30 μM)

(Figures 2a and b). As shown in Figure 2c, lysosomal Ca^{2+} release in KD cells was statistically significantly lower when compared to control cells, consistent with a reduction in lysosomal Ca^{2+} store filling when PMCA2 was defective. There was no significant difference in basal cytosolic Ca^{2+} levels in KD vs control cells (Figure 2d). As a positive control of Fura-2 response and to check neuronal excitability of differentiated PC12, cells were stimulated with 50 mM KCl. This causes a depolarisation of plasma membrane voltage-gated calcium channels in excitable cells and consequently Ca^{2+} influx from outside the cell into the cytosol, which can be measured with the Fura-2 probe. Both control and KD cells produced a significant response to KCl stimulation (Figures 2e and f), confirming the suitability of the system and that differentiation to the neuronal phenotype had occurred. There were no significant differences in KD vs controls in response to KCl stimulation (Figure 2g). As all transduced cells expressed GFP, we confirmed that GFP fluorescence did not leak into the Fura-2 channel and that there was no correlation between GFP and Fura-2 fluorescence intensities (Supplementary Figure 3).

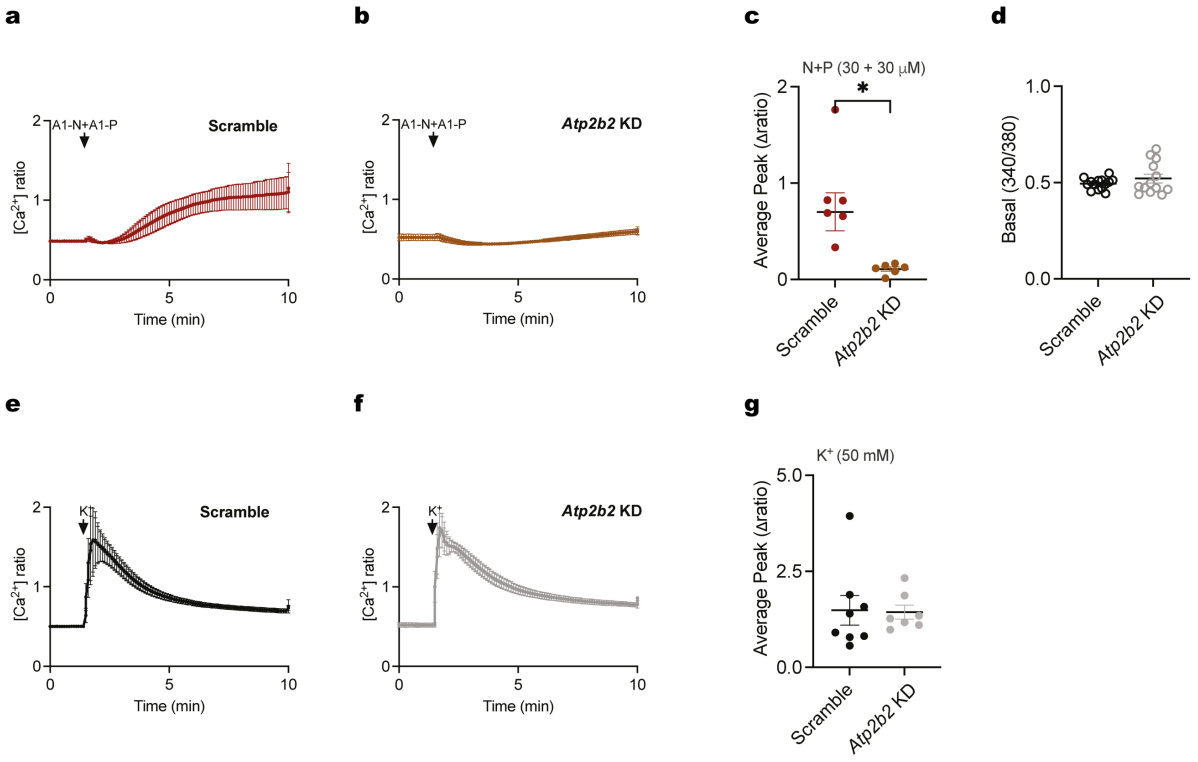

160 **Figure 2. Lysosomal Ca^{2+} content is reduced in *Atp2b2* KD cells.** PC12 cells stably
161 expressing scramble or *Atp2b2* targeting shRNA were preloaded with the Ca^{2+} probe Fura-2.
162 Ca^{2+} signal in response to a combination of the TPC2 agonists TPC2A1N (30 μM) and
163 TPC2A1P (30 μM) in scramble (a) and *Atp2b2* KD cells (b). Summary data (c) quantifying the
164 peak change in Ca^{2+} signal in scramble and *Atp2b2* KD cells stimulated with the TPC2 agonists.
165 Each point represents the mean response from > 47 cells per coverslip from three independent
166 experiments, two coverslips per experiment. (d) Basal Fura-2 signal in scramble and *Atp2b2*
167 KD cells. Each point represents the mean response from > 47 cells per coverslip from five
168 independent experiments, two to three coverslips per experiment. Ca^{2+} signal when scramble
169 (e) and *Atp2b2* KD cells (f) were depolarised with KCl (50 mM). Summary data (g) quantifying
170 the peak change in the Ca^{2+} signal in scramble and *Atp2b2* KD cells depolarised with KCl.
171 Each point represents the mean response from > 47 cells per coverslip from four independent
172 experiments, two coverslips per experiment. Lines represent the mean and standard deviation,
173 $*p < 0.05$ calculated by unpaired t-test.
174

175 **Several PMCA splice variants contain a lysosomal targeting motif.**

176 To understand how PMCA2 localises to the lysosome, we explored this and other PMCA
177 proteins in greater depth. The PMCA family in mammals comprises four genes *ATP2B1*,
178 *ATP2B2*, *ATP2B3* and *ATP2B4* that encode PMCA1, PMCA2, PMCA3 and PMCA4 proteins
179 respectively. Each contains two major splice sites, A and C, which generate multiple transcripts
180 [1]. Strikingly, we found that splicing at site C can generate transcripts that encode a canonical
181 tyrosine-based lysosomal targeting motif, YEGL. Tyrosine-based motifs are well-established
182 in mediating lysosomal trafficking, suggesting a potential mechanism for lysosomal PMCA
183 localisation [14]. Mapping the splicing patterns in human and rat revealed that several isoforms,
184 PMCA1b, 1c, 1d; PMCA2b; and PMCA3b, 3c, and 3d, retain this lysosomal targeting motif in

185 their translated sequences (Figure 3a and Supplementary Figure 4). In contrast, none of the
186 PMCA4 variants examined contained a YEGL motif, highlighting a possible isoform-specific
187 divergence in organelle targeting.
188
189 Additionally, we found that the human *ATP2B1* gene contains a Coordinated Lysosomal
190 Expression and Regulation (CLEAR) sequence in its promoter. CLEAR sequences are specific
191 E-box sites in the DNA recognised by the transcription factor TFEB to promote the coordinated
192 transcription of many lysosomal genes and plays a key role in regulating lysosome biogenesis
193 [15]. *ATP2B2* contains a CLEAR sequence between exons 1 and 2 (Figure 3a). These CLEAR
194 sequences are also present in rat with two sequences in *ATP2B1*, upstream of exon 1 and
195 between exon 1 and 2 and in *ATP2B2* between exon 1 and 2 and exon 2 and 3 (Supplementary
196 Figure 4). The CLEAR sequence in *ATP2B2* is therefore consistent with PMCA2 having a
197 lysosomal localisation.
198
199 We expanded our study from human and rat to other species and, interestingly, found that for
200 *ATP2B1*, of 100 vertebrate species' genomes collated and aligned by UCSC, all but one contain
201 a YEGL motif. The only exception was Lamprey, whose sequence is SLYEKLEKPEAR. For
202 *ATP2B2*, of the same 100 collated and aligned vertebrate species' genomes, all but two contain
203 a YEGL motif. The only exceptions were duck-billed platypus YEGI and, again, Lamprey
204 FEGF. An example of the alignment is shown in Figure 3b. The broad presence of YEGL
205 across species is indicative of a fundamental conserved role for this motif.
206
207 We also found a similar tyrosine vacuolar targeting motif, YYFL, in yeast PMC1. Interestingly,
208 in yeast and *Dictyostelium*, there is only one gene encoding p-type Ca^{2+} ATPases, *Pmc1* and

209 *patA*, respectively, with no differential splicing, that generates a vacuolar protein, suggesting

210 that PMCAs may have evolved first as lysosomal proteins [16 17].

211

212 We then generated PC12 cells that stably expressed the different splice variants of PMCA2

213 fused to GFP under a tetracycline-inducible cassette. As predicted, the PMCA2wa splice

214 variant showed a clear plasma membrane-targeted GFP signal. Interestingly, although the

215 PMCA2wb, PMCA2xb, and PMCA2zb variants, which include the YEGL motif, showed some

216 intracellular GFP localisation, they also displayed a strong plasma membrane signal when

217 overexpressed, in contrast to the lysosomal localisation of endogenous PMCA2 in PC12 cells

218 (Supplementary Figure 5).

219

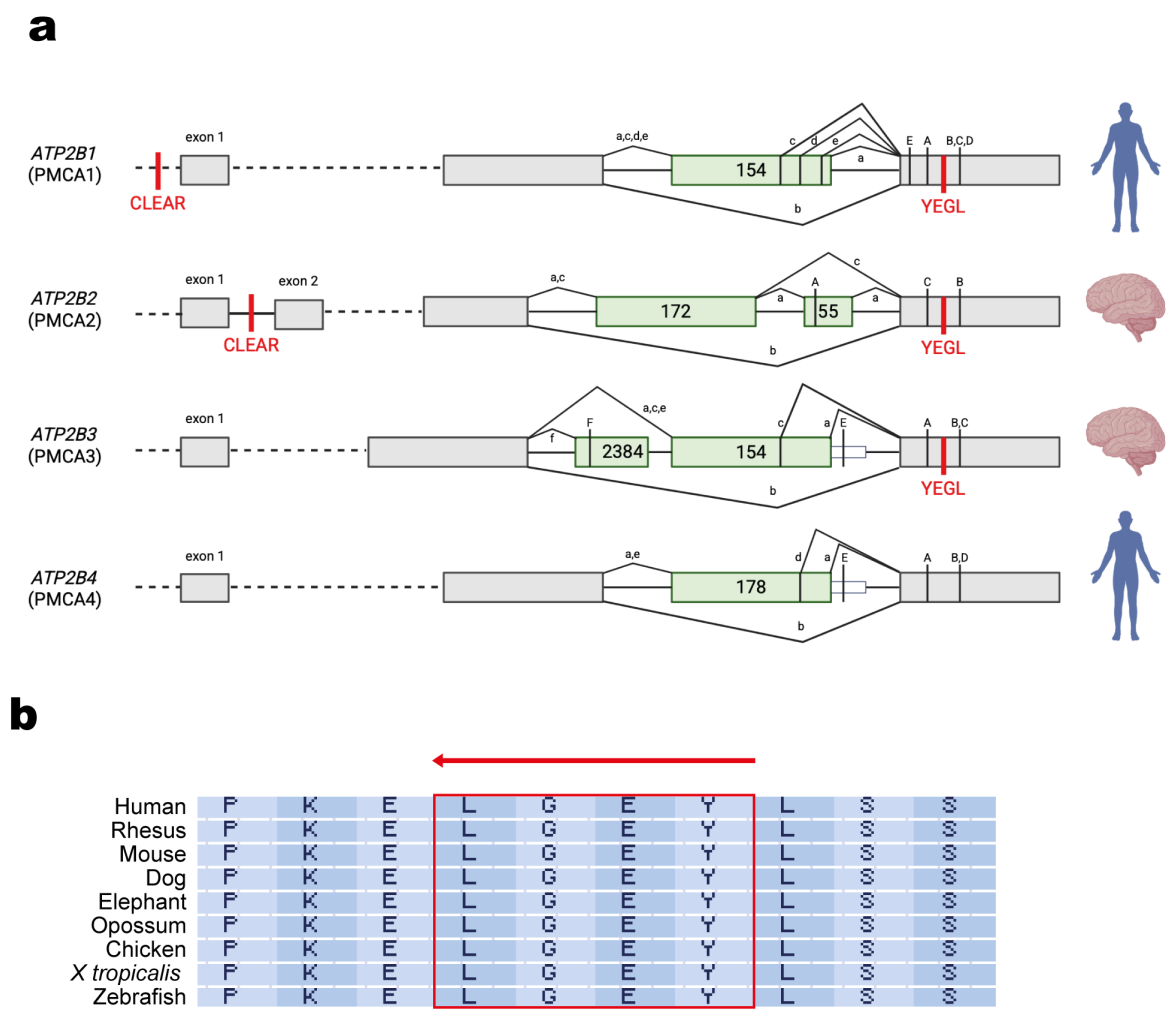

220

221

222 **Figure 3. Specific PMCA splice variants contain the lysosomal targeting motif YEGL.**
223 ***ATP2B1* and *ATP2B2* contain CLEAR sequences.** (a) PMCA site C alternative splicing in
224 human can include or exclude the lysosomal targeting motif YEGL. The exon structure of the
225 different regions affected by alternative splicing is shown for each of the four PMCA genes.
226 Constitutively spliced exons are indicated as grey boxes. Alternatively-inserted exons are
227 shown in green. Lowercase letters represent resulting splice variants. Capital letters indicate
228 the position of the translated stop codons. In PMCA3 and PMCA4, splice variant "e" results
229 from a read-through of the exon into the following intron (indicated as small white boxes). The
230 sizes of alternatively spliced exons are given as nucleotide numbers. Splice variants shown
231 have supporting sequence data in the literature, RefSeq or Ensembl at the time of submission
232 of this work. (b) Example of the YEGL motif alignment in the *ATP2B2* gene from different
233 species.

234

235 **PMCA2 knockdown induces multiple NPC cellular phenotypes.**
236 Having established that PMCA2 can localise and function in the lysosome, and that *Atp2b2*
237 (PMCA2) KD in cells produces a defect in lysosomal Ca^{2+}, a hallmark of NPC, we studied
238 whether other biochemical characteristics of NPC (Figure 4a), such as cholesterol,
239 glycosphingolipid (GSL) and sphingosine accumulation, occur in cells defective in PMCA2.
240 To study cholesterol distribution, cells stably expressing a scramble (control) or *Atp2b2* shRNA
241 (KD) were differentiated into neurons and incubated in lipoprotein-deficient serum (LPDS)
242 supplemented with low-density lipoproteins (LDL). Cells were fixed and stained with filipin,
243 a fluorescent molecule that binds cholesterol. Using confocal microscopy, we observed a
244 difference in free cholesterol distribution between the control (scramble cells) and *Atp2b2* KD
245 cells (Figure 4b). The staining was diffuse in control cells whereas in KD cells we observed

intracellular staining in puncta compatible with lysosomal accumulation of cholesterol, a hallmark of NPC. Next, PC12 cells were differentiated and sphingosine and GSLs were measured by HPLC. No differences were found in sphingosine levels (Figure 4c). However, GM1a-Gc, GD1a, GD1b and GlcCer accumulated in *Atp2b2* KD cells (Figure 4d), but no differences were found for GT1b (Figure 4d).

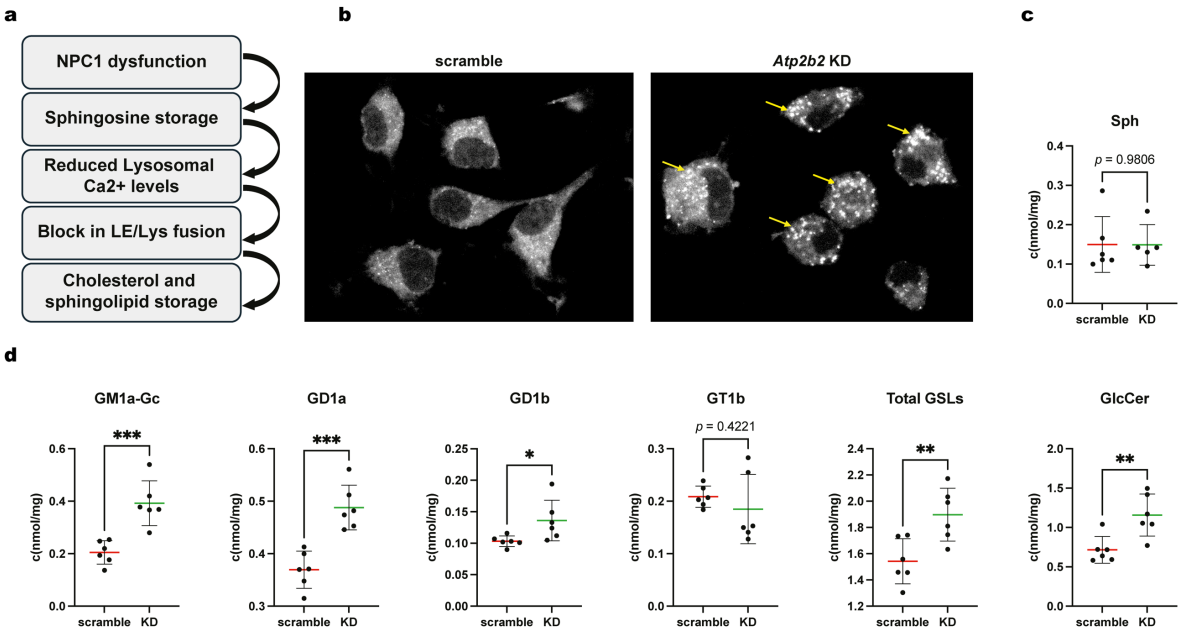

Figure 4. *Atp2b2* deficiency induces multiple NPC phenotypes but not sphingosine storage. (a) Diagram of the proposed NPC pathogenic cascade[8]. (b) Filipin staining of free cholesterol in scramble and *Atp2b2* KD cells, representative image of 3 independent experiments. Sphingosine (c) and GSLs (d) concentrations in scramble vs *Atp2b2* KD cells, (n = 6 scramble and 5 KD for sphingosine, due to the exclusion of an outlier detected using Grubbs' test; n = 6 for GSLs). Lines represent the mean and standard deviation, *$p < 0.05$, **$p < 0.01$, ***$p < 0.001$ calculated by unpaired t test.

NPC1 KO leads to reduced *Atp2b2* (PMCA2) splice variant expression in the mouse brain.

263 We previously reported that *Atp2b2* (PMCA2) gene expression was reduced in the cerebellum
264 of the *Npc1*$^{-/-}$ mice an NPC model that recapitulates the biochemical and phenotypic features
265 of the human disease [7]. To further investigate the contribution of each *Atp2b2* splice variant to
266 this reduction, *Atp2b2* expression was measured in the cerebellum of the *Npc1*$^{-/-}$ mouse. First,
267 using PCR and gel electrophoresis, we found that the predominant splice variant in mouse
268 cerebellum is PMCA2b containing the YEGL lysosomal targeting motif, followed by PMCA2a
269 (Figure 5a). The expression of the transcript encoding PMCA2c was too low to be detected by
270 PCR. To accurately measure differences in splicing in *Npc1*$^{-/-}$ vs wild-type mice (WT), we used
271 quantitative PCR (qPCR). All *Atp2b2* splice variants were downregulated in *Npc1*$^{-/-}$ mice
272 compared to WT, with a 67.1 % overall reduction (Figure 5b).
273

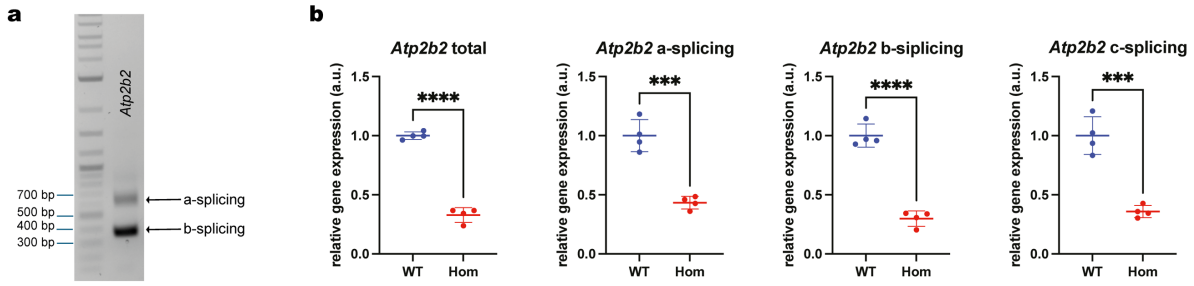

274
275

276 **Figure 5. Npc1 deficiency reduces *Atp2b2* splice variant expression.** (a) Gel electrophoresis
277 of PCR products showing the relative abundance of the different *Atp2b2* splice variants in the
278 cerebellum of 8-week-old WT mice. (b) Relative gene expression measured by qPCR of
279 different splice variants of *Atp2b2* in WT and *Npc1*$^{-/-}$ (Hom) cerebellums of 8-week-old *Npc1*$^{-}$
280 $^{/-}$ mice, $n = 4$ mice. Lines represent the mean and standard deviation, ***$p < 0.001$, ****$p <$
281 0.0001 calculated by unpaired t test.
282

283 Many genes causative of lysosomal storage diseases, including *NPC1*, have been found in the
284 heterozygous state to be over-represented in Parkinson's disease [18]. We therefore investigated

285 whether mRNA levels of *NPC1* and its interacting partners (including PMCA2) were altered
286 in Lewy body diseases.
287
288 **The splicing of PMCAs is altered in Lewy body diseases with implications for PMCA**
289 **lysosomal targeting and function.**
290 To evaluate the expression and splicing of *ATP2B2* (PMCA2) across Lewy body diseases
291 (LBD), we analysed data from a study applying single-nucleus (snRNA) and bulk-tissue RNA-
292 sequencing to human post-mortem anterior cingulate cortex tissue from 28 individuals[19]. This
293 cohort included four groups consisting of healthy controls, Parkinson's disease (PD),
294 Parkinson's disease with dementia (PDD) and dementia with Lewy bodies (DLB), based on
295 clinical assessments of retrospectively reviewed case records ($n = 7$ per group). Using snRNA-
296 seq data we identified statistically significant reductions in gene expression in several cell types
297 in PD, PDD and DLB (Figure 6a). Notably, downregulation of *ATP2B2* expression was
298 consistent in excitatory neurons across the three disorders, with less consistent downregulation
299 across multiple glial cell types. These included reduced expression of *ATP2B2* in
300 oligodendrocyte precursor cells (control vs PD, FDR-adjusted $p = 0.031$, Log2FC = -1.1),
301 oligodendrocytes (control vs PDD FDR-adjusted $p < 0.05$, Log2FC = -0.68; control vs DLB,
302 FDR-adjusted $p < 0.001$, Log2FC = -3.5), and microglia (control vs DLB, FDR-adjusted $p <$
303 0.01, Log2FC = -3.1).
304
305 Given these findings, we extended the analysis to included *NPC1* and other genes encoding
306 confirmed or potential NPC1 interacting partners based on the literature [7 20 21 22]. We also
307 analysed the expression of other genes implicated in the NPC pathway (Figure 6a). Of the 21
308 genes of interest, we found that 13 were differentially expressed in at least one cell type or
309 disease state (Figure 6a). Consistent with the *ATP2B2* data, most changes were seen in

310 excitatory neurons and oligodendrocytes when focusing on DLB. Interestingly, the gene *FTH1,*
311 which is involved in iron metabolism showed downregulation in a broader range of cell types.
312
313 Next, we leveraged the availability of high-depth bulk RNA-seq data, and while we identified
314 no significant change in the expression of PMCA genes, given the importance of splicing for
315 the regulation of PMCA gene function/localisation, we investigated changes in transcript use
316 across disease states. We assessed differential splicing of all the PMCA genes as well as genes
317 identified as confirmed and potential interactors of NPC1 (Figure 6b). A gene was counted as
318 differentially spliced if it contained one or more differentially spliced clusters within its locus.
319 Interestingly, we found that 10 of the 21 genes of interest were significantly differentially
320 spliced when control samples were compared to PD, PDD and DLB sample sets. This gene set
321 included *ATP2B2*, *ATP2B1* and *NPC1*, which all showed evidence of significant differential
322 splicing across all Lewy body diseases.
323
324 However, we were particularly interested in splicing events that could impact on the inclusion
325 of the YEGL motif in members of the PMCA gene family. Specifically, we assessed changes
326 in *ATP2B2* splicing that would affect lysosomal targeting of the protein by calculating the
327 difference in the inclusion (delta percent spliced in (ΔPSI)) of specific 3' junctions found
328 uniquely in either the variant-a and -b transcripts. We found increased use of variant-b
329 junctions that would be predicted to include the lysosomal targeting sequence increased in use
330 in PD (FDR-adjusted $p < 0.001$; ΔPSI=37%). In DLB we noted a significant downregulation
331 of this junction type in *ATP2B2* (FDR-adjusted $p < 0.01$; ΔPSI=-6%; Figure 6c). These splicing
332 changes indicate there are dynamic changes in *ATP2B2* splicing across Lewy body diseases,
333 and this was further evidenced by splicing changes of *ATP2B1* and *ATP2B4* in these diseases,
334 indicating potential alterations in lysosomal targeting (Supplementary Table 1). Together,

these findings suggest that changes in PMCA splicing and lysosomal targeting play a role in Lewy body diseases.

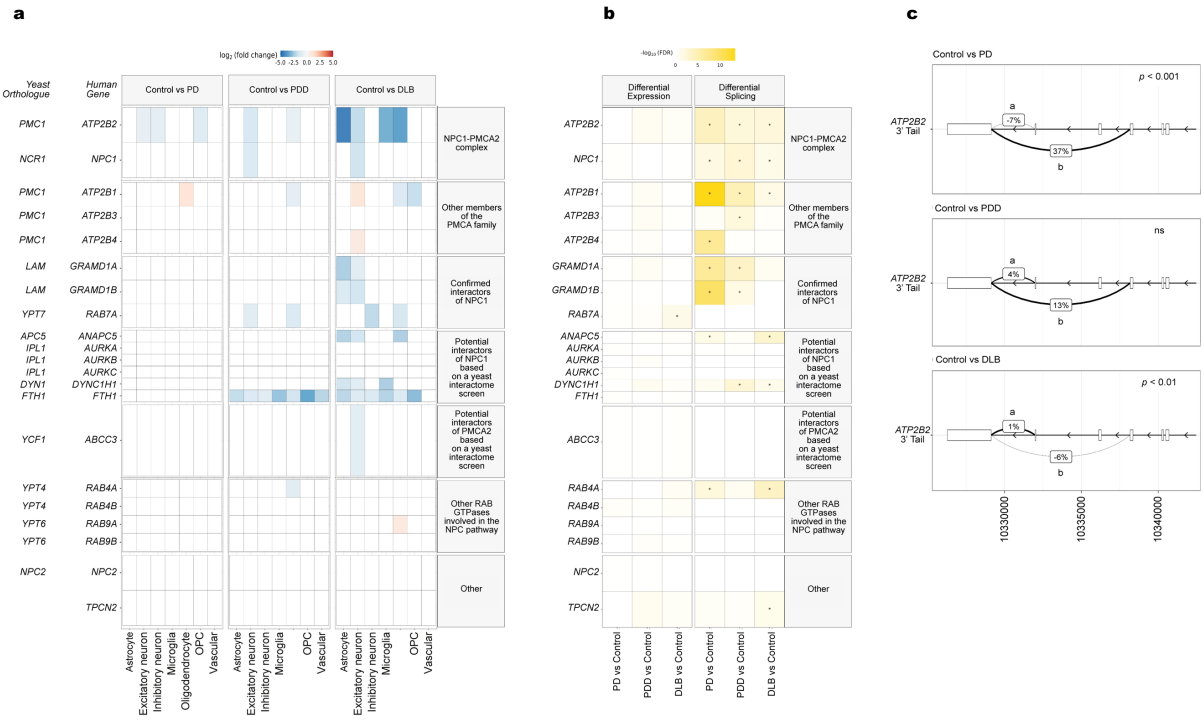

Figure 6. PMCA2, NPC1 and their wider interactome gene expression and splicing are altered in Lewy body diseases. (a) Gene expression changes using single-nucleus RNA sequencing in post-mortem human brain samples from PD, PDD and DLB cases and controls. Fill of the tile indicates the significant (FDR < 0.05) log2(fold change), with non-significant results (FDR > 0.05) coloured white. (b) Gene expression and differential splicing of *NPC1* and potential NPC1 interacting partners using bulk RNA sequencing in PD, PDD and DLB compared to controls. The fill colour of each tile represents the −log10(FDR) for the gene (left panel) or the most significant spliced junction cluster within each gene (right panel), with FDR significance <0.05 indicated by an *. (c) *ATP2B2* splice variants demonstrate differential splicing profiles in Lewy body disorders. Sashimi plots showing delta percent spliced in comparison to controls for junctions producing alternative *ATP2B2* splice variants a and b. (a)

351 *n* = 7 patients per group. (b and c) *n* = 5 controls, *n* = 7 PD, *n* = 6 PDD and *n* = 6 DLB. PD:
352 Parkinson's disease, PDD: PD with dementia, DLB: dementia with Lewy bodies.
353
354 **Discussion**
355 In this study, we surprisingly found that PMCA2 localises to the lysosome. A possible
356 explanation for this unexpected localisation of PMCA is the presence of a canonical tyrosine-
357 based lysosomal targeting motif (YEGL), which we identified in specific splice variants of
358 PMCA genes. In addition, both PMCA1 and PMCA2 harbour CLEAR (Coordinated
359 Lysosomal Expression and Regulation) elements, further supporting a lysosomal role for these
360 isoforms. Notably, the YEGL motif was conserved across 98% of the 100 species examined,
361 suggesting it plays a fundamental and evolutionarily conserved role. Intriguingly, orthologues
362 of PMCAs in yeast and *Dictyostelium* localise to the vacuole, the equivalent of the lysosome
363 in these organisms, raising the possibility that plasma membrane targeting of PMCAs may have
364 evolved secondarily to an ancestral lysosomal localisation and function.
365
366 Interestingly, when PMCA2 splice variants containing the lysosomal targeting motif were
367 overexpressed, they localised not only to intracellular compartments but also to the plasma
368 membrane. This dual localisation suggests that intracellular retention may require interaction
369 with specific partner proteins in the lysosome. In the absence of sufficient binding partners,
370 may, by default, insert in the plasma membrane, raising the possibility that stoichiometric
371 balance with interacting partners such as NPC1 also affects its subcellular distribution.
372
373 Our results are consistent with the hypothesis that the function of PMCA2 at the lysosomal
374 membrane is to complex with NPC1, which tethers the lysosome to the ER [20] and that, then,
375 PMCA2 fills the lysosome with Ca^{2+} at lysosome: ER contact sites. The lysosome is a regulated

376 Ca^{2+} store and signalling hub. Lysosomal Ca^{2+} release is needed for vesicular trafficking,
377 endosome/lysosome fusion, and phagocytosis [23]. Several proteins have been described to
378 facilitate calcium release from the lysosome, such as the TPC2 and TRPML1 channels [23] but
379 the mechanisms for lysosomal Ca^{2+} filling remain incompletely understood [24]. TMEM165 has
380 recently emerged as a candidate [25] [26]. However, it has long been speculated that both passive
381 and active Ca^{2+} transporters would be required [27]. Our study presents PMCA2 as an additional
382 candidate for lysosomal Ca^{2+} filling, specifically at NPC1-mediated contact sites between the
383 lysosome and ER.
384 After demonstrating its lysosomal localisation and interaction with NPC1 [7], we modelled its
385 orientation in the limiting membrane of the lysosome. Our results using AlphaFold favoured
386 an orientation compatible with transporting calcium into the lysosome. Consistent with this,
387 when PMCA2 was stably knocked down, the release of Ca^{2+} from the lysosome induced by the
388 TPC2 agonists TPC2-A1-N and TPC2-A1-P was significantly reduced compared to control
389 cells. These results are compatible with lower levels of lysosomal Ca^{2+} when PMCA2 is
390 defective, supporting a role for PMCA2 in mediating lysosomal Ca^{2+} filling. However, our
391 measurements were indirect, relying on monitoring cytosolic Ca^{2+} upon opening of a lysosomal
392 ion channel as opposed to direct measurements of Ca^{2+} within the lysosomal lumen. The latter
393 is challenging due to the acidic interior of lysosomes. Nevertheless, lysosomal calcium filling
394 by PMCA2 clearly merits further investigation.
395
396 When NPC1 is defective, the first event in the pathogenic cascade is the accumulation of
397 sphingosine that leads to the reduction of lysosomal Ca^{2+} levels [8]. The fact that in cells with
398 functional NPC1, knockdown of PMCA2 does not result in the accumulation of sphingosine is
399 consistent with NPC1-dependent sphingosine transport being upstream of the lysosomal Ca^{2+}
400 defect. Our discovery that PMCA2 expression is reduced in *Npc1*-null mice links this Ca^{2+}

401 transporter to the NPC pathway, explaining for the first time why lysosomal Ca^{2+} levels are
402 reduced when NPC1 is defective. This hypothesis is further supported by the fact that when we
403 knockdown PMCA2, lysosomal Ca^{2+} levels are also reduced. Another link between PMCA2
404 and the NPC pathway is that in cells with intact NPC1 but reduced levels of PMCA2, lipids
405 such as cholesterol and the majority of GSLs accumulate, as observed in NPC cells. These data
406 suggest that the NPC1/PMCA axis is a hub regulating lysosomal Ca^{2+} and lipid homeostasis at
407 NPC1 mediated contact sites between the lysosome and ER.
408 It is interesting that mutations in PMCA2 in humans and mouse models lead to ataxia [2,3],
409 another characteristic phenotype of NPC. Interestingly, PMCA2 is highly expressed in the
410 cerebellum, particularly in Purkinje neurons, a cell type that is uniquely susceptible to
411 degeneration in NPC [28].
412
413 Importantly, the reduction in PMCA2 gene expression was not limited to NPC but was also
414 observed in several cell types in PD, PDD, and DLB. This is highly relevant as it has been
415 reported that a reduction in *ATP2B2* (PMCA2) increases neuronal vulnerability in *in vitro* PD
416 models [5]. In this study, we found that a reduction in PMCA2 leads to GSL dyshomeostasis,
417 that has also been reported in PD [29 30]. Furthermore, low lysosomal Ca^{2+} levels have also been
418 reported in PD [9 24]. Since mutations in NPC1 are overrepresented in PD [18], taken together with
419 our findings in this study, we hypothesise that the NPC1-PMCA2 complex is part of a wider
420 interactome in the lysosome whose dysregulation plays a key role in NPC and Lewy body
421 pathologies. Supporting this hypothesis, gene expression of *NPC1, ATP2B2* and several of their
422 confirmed and potential binding partners are also dysregulated in different brain cell types in
423 Lewy body diseases.
424

425 A key finding in this study was a profound PD-related change in splice variant usage in several
426 members of the wider NPC1 interactome. Changes in the splice variant expressed could,
427 potentially, change the protein localisation, regulation or function in the disease state. This
428 result highlights the need for more comprehensive studies that include not only total expression
429 but also differential splice variant usage.
430
431 In conclusion, our study uncovers for the first time a previously unrecognised, differential
432 splicing-dependent role for PMCA2 involved in lysosomal Ca^{2+} filling, expanding the known
433 functions of the PMCA family beyond its canonical activity at the plasma membrane. We show
434 that alternative splicing directs specific PMCA2 isoforms to the limiting membrane of the
435 lysosome, where they interact with NPC1 to restore luminal Ca^{2+} levels. This mechanism is
436 essential for lysosomal function, and its disruption results in lysosomal Ca^{2+} depletion and lipid
437 accumulation, features common to Niemann-Pick disease type C and Parkinson's disease.
438 These findings define a novel function for the NPC1–PMCA2 complex in lysosomal Ca^{2+}
439 homeostasis and highlight how alternative splicing can diversify the functional landscape of
440 well-characterised genes. More broadly, our work underscores the importance of isoform-
441 specific regulation in organelle biology and opens new avenues for understanding and targeting
442 lysosomal dysfunction in neurodegenerative diseases.
443
444
445
446
447
448
449

450

451

452

453 **Materials and Methods**

454

455 **Materials**

456 RPMI 1640 culture medium was obtained from Sigma. Foetal bovine serum (FBS), horse
457 serum and Glutamax for supplementing the medium were obtained from Gibco. NGF-β from
458 rat (N2513), and the antibiotics penicillin and streptomycin were obtained from Sigma.

459

460 **Low-density lipoprotein (LDL) and lipoprotein-deficient serum (LPDS) preparation**

461 Human LDL (1.019–1.063 kg/l) was isolated by vertical rotor density gradient
462 ultracentrifugation of plasma from hypercholesterolemic patients, as previously described [31].
463 LPDS was prepared from FBS by ultracentrifugation at a density of 1.21 kg/l [31].

464

465 **Cells**

466 PC12 cells (ATCC CRL-1721) were maintained in RPMI 1640 supplemented with 10% horse
467 serum, 5% FBS, 2 mM L-alanyl-L-glutamine dipeptide in 0.85% NaCl (Glutamax), 100 U/ml
468 penicillin and 100 U/ml streptomycin at 37 °C, in humidified atmosphere with 5% CO2. For
469 differentiation to neurons, PC12 cells were plated onto poly-D-lysine-coated coverslips or
470 flasks and incubated in RPMI 1640 supplemented with 1% horse serum, 100 ng/ml NGF-β and
471 the abovementioned additives for four days. Medium was replaced on the second day.
472 For cholesterol distribution experiments, after differentiation, PC12 neurons were pre-treated
473 with RPMI 1640 supplemented with 10% LPDS for 24 h. Subsequently, LDL (40 µg/ml

474 cholesterol) was added to the culture. After 24 h, cells were fixed with 4% paraformaldehyde
475 in PBS.
476
477
478 **Generation of stable *Atp2b2* KD and scramble PC12 cells**
479 Lentiviral particles were prepared by transfecting HEK293T cells with Gag-Pol and pMDG
480 packaging plasmids, and each of four rat *Atp2b2* or scrambled shRNA plasmid (TL709157,
481 Origene). PC12 cells were transduced with the lentiviral constructs for 24 h. Then, we
482 performed a kill curve with puromycin. After puromycin selection, *Atp2b2* expression was
483 assessed by qPCR. Cells transduced with the shRNA leading to the greatest reduction (> 80%)
484 of *Atp2b2* gene expression and scrambled shRNA cells were selected for further experiments.
485
486 **Animals**
487 All experiments were conducted using protocols approved by the UK Home Office Animal
488 Scientific Procedures Act, 1986. All animal work followed the ARRIVE guidelines.
489 BALB/cNctr-Npc1^{m1N}/J also named *Npc1^{nih}* mice, were generated by heterozygote
490 brother/sister matings obtained from Jackson Laboratory (Charles River, UK). Mice were bred
491 and housed in individually ventilated cages (IVCs) under non-sterile conditions. Mice were
492 culled at eight weeks of age with 800 mg/kg pentobarbital IP. For biochemical analysis, mice
493 were transcardially perfused with ice-cold PBS and their brains removed and dissected.
494
495 **Microscopy**
496 PC12 cells were plated onto poly-D-lysine-coated coverslips and differentiated into neurons
497 over four days. Then cells were fixed with 4 % paraformaldehyde for 10 min and permeabilised
498 with 0.1 % saponin in PBS for 1 hour at room temperature (RT). Cells were blocked with 10%

499 horse serum in PBS for 1 hour. Primary polyclonal PMCA2 (PA1-915, Invitrogen) and
500 monoclonal NPC1 (ab134113, abcam) antibodies were labelled with Flexable Coralite Plus-
501 555 (KFA502, proteintech) and Flexable Coralite Plus-488 (KFA501, proteintech) for rabbit
502 antibodies following the manufacturer's instructions. Cells were probed with the conjugated
503 antibodies overnight at 4ºC, washed and mounted on slides using Prolong Gold mounting
504 medium. Alternatively, after differentiation and incubation with LPDS and LDL as described
505 above, PC12 neurons were fixed with 4% paraformaldehyde for 10 min and exposed to filipin
506 (35 µg/ml in PBS) for 1 h. After washing, coverslips were mounted on slides with ProLong
507 Gold. Confocal images were acquired using a Leica-SP8 confocal microscope with an LD 63X
508 objective.
509
510 All image analysis were performed using ImageJ (FIJI) software (version 2.16.0/1.54g,
511 ImageJ2). For quantification of colocalisation of NPC1 and PMCA2, the JACoP plugin [32] was
512 used.
513
514

515 **Tagless LysoIP**

516 Tagless LysoIP was performed as described by Saarela et al. [12] with minor modifications.
517 Briefly, mouse cerebellum (whole cerebellum per data point) were collected and gently
518 homogenised with 40 strokes of an electric homogeniser in 1 ml of potassium phosphate buffer
519 saline (KPBS) supplemented with Halt protease inhibitor cocktail (Thermo Fisher Scientific)
520 and PMFS (Cell Signaling Technology). Samples were centrifuged at 1000 g for 2 min at 4ºC.
521 Supernatant was collected, and 50 µl was reserved as input (whole tissue extract). The rest of
522 the supernatant was divided into two tubes, each containing 100 µl of magnetic beads bound
523 to antibodies against murine TMEM192 or isotype IgG. Magnetic beads were previously
524 washed with KPBS. Supernatants were incubated with the magnetic beads for 5 min at 4ºC on
525 an orbital shaker. After incubation, the mixture was placed on a magnet for 1 min and the
526 supernatant was removed. The beads were washed 3 times with ice cold KPBS supplemented
527 with the protease inhibitors. Ripa buffer (Cell Signaling Technology) plus protease inhibitors
528 was added to the beads and input. Samples with beads were placed on a magnet, and lysates
529 were collected for western blot.

530

531 **Western blotting**

532 Cells and lysoIP fractions were lysed in Ripa Buffer (Cell Signaling Technology)
533 supplemented with a Halt™ protease inhibitor cocktail (Thermo Fisher Scientific) and PMFS
534 (Cell Signaling Technology). Protein expression was measured using the bicinchoninic acid
535 method (BCA Protein Assay Kit, Pierce). Lysates were separated on 4–12% SDS–PAGE gels
536 (Thermo Fisher Scientific) and then transferred to PVDF membranes. For Western blot
537 normalisation, we used the Revert™ 700 Total Protein (LI-COR). After destaining, membranes
538 were blocked with TBS-Intercept blocking buffer (LI-COR) and probed with primary
539 polyclonal anti-PMCA2 (PA1-915, Invitrogen) antibody and secondary antibodies conjugated

540 to IRDye 800CW (LI-COR). Fluorescence was detected using an Odyssey M scanner (LI-
541 COR). Acquired images were visualised and quantified with the Empiria Studio Software (LI-
542 COR).
543
544 **qPCR**
545 Total RNA from mouse brain was isolated using the RNAeasy plus extraction kit (Qiagen)
546 following the manufacturer's protocol. cDNA was synthesised using the iScript cDNA
547 synthesis kit (BIO-RAD). Real-time PCR amplification was performed on a LightCycler 480
548 II, using the PowerUp SYBER Green (Thermo Fisher Scientific), and specific primers
549 (Supplementary table 2). Relative expression of each gene was determined by calculating the
550 increase in CP (ΔCP) and normalising by the housekeeping gene Rpl37 (ribosomal protein
551 L37).
552
553 **GSLs analysis**
554 Glucosylceramide (GlcCer) and downstream GSLs were analysed as previously described [33]
555 with minor modifications. Detailed protocols are available at protocols.IO for GlcCer and
556 GSLs [34] determination. Briefly, GSLs were extracted from cell homogenates (200 µg of
557 protein) in C:M 1:2 overnight. The mixture was centrifuged, chloroform and PBS were added
558 to the supernatant and centrifuged. The lower phase was dried and resuspended in a small
559 volume of C:M 1:3 and mixed with the upper phase. GSLs were recovered using C18 Isolute
560 columns (100 mg, Biotage), and three quarters of the column elutant was dried and resuspended
561 in ceramide glycanase buffer (50 mM sodium acetate pH 5.5, 1 mg/mL sodium
562 taurodeoxycholate). rECGase 1 (prepared by Genscript) was added and samples incubated
563 overnight. The other quarter of the column elutant was also dried and resuspended in ceramide
564 glycanase buffer, but Cerezyme® (Genzyme, Cambridge, MA) was added and incubated for

565 72 h. Released lipids were anthranilic acid (2-AA) labelled and purified on Discover DPA-6S
566 SPE columns (SUPELCO). Lipids were eluted in H_2O and loaded 60:140 H_2O: MeCN (v/v)
567 for normal phase high-performance liquid chromatography (NP-HPLC). The NP-HPLC
568 system consisted of a Waters Alliance 2695 separations module and an in-line Waters 2475
569 multi λ-fluorescence detector set at Ex λ 360 nm and Em λ 425 nm. The solid phase used was
570 a 4.6 × 250 mm TSK gel-Amide 80 column (Tosoh Bioscience). A 2AA-labelled glucose
571 homopolymer ladder (Ludger, UK) was included to determine the glucose unit values (GUs)
572 for the HPLC peaks. Individual GSL species were identified by their GU values and quantified
573 by comparison of integrated peak areas with a known amount of 2AA-labelled BioQuant
574 chitotriose standard (Ludger, UK). Results for cell homogenates were normalised to protein
575 content, determined by the bicinchoninic acid (BCA) assay.
576
577 GSL species identification and concentration quantification were performed using the software
578 HPLC-RS (https://github.com/ArchercatNEO/HPLC/tree/v0.9).
579
580 **Sphingosine analysis by HPLC**
581 Detailed protocol is available at protocols.IO [35]. Briefly, sphingoid bases were extracted from
582 homogenised cells (0.2 mg protein) in 100 µL H_2O and spiked with an internal standard (C20,
583 3 µL 0.03 mM). To the homogenate, 500 µL C:M 1:2 was added and sonicated for 10 minutes,
584 RT. To the samples, 500 µL 1 M NaCl, 500 µL chloroform, and 100 µL 3 M NaOH were added
585 and incubated for 15 minutes, RT, and vortexed every 5 minutes. Samples were then
586 centrifuged (16 000 g/10 minutes) and the lower phase purified on SPE NH2 columns (Biotage)
587 pre-equilibrated with 2 × 1 mL chloroform and eluted with 900 µL acetone. The column elutant
588 was then dried down under N_2 and resuspended in 50 µL pre-warmed HPLC-grade EtOH.
589 Sphingoid bases were labelled with 50 µL OPA labelling solution (o-phtalaldyhyde dissolved

590 in 20x EtOH, 1× 2-mercaptoethanol and diluted in 2000× 3% boric acid pH 10.5) and incubated
591 in the dark at 20ºC for 20 minutes, vortexing at 10 minutes intervals. Samples were buffered
592 in 100 µL MeOH:5 mM Tris pH 7 9:1, centrifuged (800 g / 2 min), and the supernatant was
593 loaded for reverse phase HPLC. Solvent A was MeOH, solvent B was H_2O, solvent C was
594 MeCN, and solvent D was MeCN:H_2O 1:4. The RP-HPLC system consisted of a VWR Hitachi
595 Elite LaChrom HPLC system with a L-2485 fluorescence detector set at Ex λ340nm and Em
596 λ455nm. The solid phase used was a Chromolith Performance RP-18e 100–4.6 HPLC column
597 (Merck, Darmstadt, Germany). Results were normalised to protein content.
598
599 **Processing of human brain RNA-seq data**
600 FASTQ files from a publicly available dataset on Lewy body diseases (PMID: 34309761),
601 containing samples from the frontal cortex of 7 PD, 6 PDD, 6 DLB and 5 age-matched non-
602 neurological control individuals, was run through a Nextflow [36] pipeline that performed quality
603 control (QC) of reads and aligned the samples to the human genome and transcriptome
604 (GRCh38 and Gencode v41 annotations [37]). Briefly, initial QC was performed using fastp
605 (v0.23.2 [38]), which removed low quality reads and bases, as well as the trimming of adapter
606 sequences. Filtered reads were aligned to the transcriptome using Salmon (correcting for
607 sequence-specific, fragment GC-content and positional biases; v1.9.0 [39]) using the entire
608 genome as a decoy sequence. For splicing analyses, reads were aligned to the genome using
609 STAR (v2.7.10a, with two-pass mode). FastQC (v0.11.9 [40]) was used to generate read QC data
610 before and after fastp filtering. RSEQC (v4.0.0 [41]), Qualimap (v2.2.2a [42]) and Picard (v2.27.5
611 [43]) were used to generate alignment QC metrics. MultiQC (v1.13 [44]) was used to visualise and
612 collate quality metrics from all pipeline modules. Full details for the pipelines and parameters
613 used for each module can be found in (Brenton [45]):
614 https://github.com/Jbrenton191/RNAseq_splicing_pipeline.

615 Transcriptome aligned reads generated from Salmon were used to identify covariates. Salmon
616 read files were imported into R (v4.3.0) and converted into gene-level count matrices using the
617 tximport (v1.30.0) and DESeq2 (v1.42.1) packages.
618 Sample and sequencing covariates were assessed for collinearity using a custom script to
619 reduce the number of covariates tested. This employed the stats (v4.2.3) and Hmisc (v5.2-0)
620 packages to generate Spearman correlations, Kruskal-Wallis and chi-square tests to assess
621 relationships between covariates. Of the numeric covariates that were collinear, those with the
622 lowest overall correlations to all other variables were kept. VariancePartition (v1.32.5) scoring
623 and correlations between remaining covariates and the top 10 principal components (PCs) were
624 then used to assess which covariates should be controlled for in the final analysis.
625
626

627 **DESeq2 differential gene expression**

628 Differential gene expression analysis was performed with DESeq (v1.42.1) using covariates
629 generated as above. Genes with 0 counts in at least one sample in all of the case or control
630 groups, as well as any gene overlapping ENCODE blacklist regions of the genome were
631 removed prior to analysis. Genes were classified as significantly upregulated if their Benjamini
632 and Hochberg FDR adjusted p value was ≤ 0.05 and Log2 fold change was > 0, and
633 significantly downregulated if their FDR ≤ 0.05 and Log2 fold change was < 0.

634

635 **Single nuclear gene expression analysis of PMCA family and NPC1 interactome**

636 Publicly available processed single nuclear gene expression results from the same samples as
637 used for above bulk gene expression (PMID: 34309761) were downloaded and interrogated for
638 significant changes in genes in the PMCA and NPC1 family of genes and their interaction
639 partners. All quality control, alignment and differential expression analysis measures are
640 described in (PMID: 34309761).

641

642 **Differential splicing of bulk RNAseq data from human brain**

643 Leafcutter (0.2.9 [46]) was used to perform differential splicing. SJ.out files containing junction
644 reads were first converted to junction files with junctions overlapping ENCODE blacklist
645 regions removed using a custom R script. Junction files were then clustered using the
646 leafcutter_cluster.py script from the leafcutter authors. The following options were used to
647 remove junctions/introns with the following criteria: junctions supported by < 30 reads across
648 all samples, supported by $< 0.1\%$ of the total number of junction read counts for the entire
649 cluster and larger than 1 Mb.

650 Pairwise group comparisons, correcting for identified covariates, were made using Leafcutter's
651 differential splicing.R function with the following options: intron clusters with more than 40

652 junctions and a coverage of ≤ 20 reads in ≤ 3 samples in per group were removed, as well as
653 individual introns that were not found in ≥ 5 samples. Clusters were considered significant if
654 they had an FDR-corrected *p* value of ≤ 0.05.
655 *ATP2B2* splice variant analysis was performed by comparing the delta percent spliced in or
656 delta usage of specific junctions representing splice variants a and b in *ATP2B2* between cases
657 and controls. The coordinates for a variants are start:10329125 and end: 10331983 and
658 start:10329125 and end: 10338176 for b variants.
659
660 **Plot generation**
661 Plots were made using ggplot (v3.5.1) and ggtranscript (v0.99.9).
662
663 **Conserved Sequence Alignment**
664 Cross-species amino acid and nucleotide alignments were inspected via the UCSC Genome
665 Browser (https://genome.ucsc.edu/cgi-bin/hgTrackUi?g=cons100way) [47] using hg19 human
666 and rn6 rat genome assemblies.
667
668 ***In vitro* cytosolic calcium measurements using Fura-2**
669 PC12 cells plated on poly-D-lysine coverslips and differentiated to neurons were loaded with
670 the ratiometric fluorescent Ca^{2+} indicator Fura-2 by incubation for 1 h at RT with the
671 acetoxymethyl ester form of Fura-2 (Fura-2 AM, 2.5 µM) and 0.005% (vol/vol) pluronic acid
672 (both from Invitrogen) in HEPES-buffered saline (HBS) containing 10 mM HEPES, 1.25 mM
673 KH_2PO_4, 2 mM $MgSO_4$, 3 mM KCl, 156 mM NaCl, 2 mM $CaCl_2$, and 10 mM glucose (all
674 from Sigma-Aldrich) at pH 7.4. After labelling, cells were washed three times in HBS and
675 mounted in an imaging chamber (Bioscience Tools) with 1 ml HBS.
676

677 Epifluorescence images were captured every 3 s with a Megapixel monochrome cooled
678 coupled device camera attached to an Olympus IX73 inverted fluorescence microscope that
679 was fitted with a 20X objective, and a Cairn CoolLED multiple wavelength LED source under
680 the control of MetaFluor 7.10.3.279 software. The Fura-2 ratio was recorded using dual-
681 excitation wavelengths of 340 and 380 nm, and a 440-nm long-pass filter was used to collect
682 emitted fluorescence. GFP-tagged constructs were identified by excitation at 488 nm and
683 capturing emitted fluorescence using a 515 nm long-pass filter.
684
685 PC12 neurons were depolarised by replacing HBS with high-potassium buffer, containing 10
686 mM HEPES, 1.25 mM KH_2PO_4, 2 mM $MgSO_4$, 156 mM KCl, 3 mM NaCl, 2 mM $CaCl_2$, and
687 10 mM glucose (all from Sigma-Aldrich) at pH 7.4 such that the final KCl concentration was
688 50 mM. Cells were also acutely challenged with a combination of the TPC2 agonists TPC2-
689 A1N and TPC2-A1P, both at 30 μM.
690
691 **AlphaFold3 structure predictions**
692 All protein models were generated using AlphaFold 3 accessed via the AlphaFold Server with
693 default settings (https://alphafoldserver.com/) [48]. Proteins modelled included human NPC1
694 (UniProt ID: O15118-1), human PMCA2 (UniProt ID: Q01814-1), yeast Ncr1 (UniProt ID:
695 Q12200-1), and yeast Pmc1 (UniProt ID: P38929-1). Graphical representations of the predicted
696 protein complex structures were prepared using PyMOL (Schrödinger LLC).
697
698 **Statistical analysis**
699 To analyse PMCA2 enrichment in the lysosomal fraction following Tagless LysoIP
700 experiments, we performed a one-way Anova analysis, followed by a Tukey's multiple
701 comparisons test with a 95% confidence interval. Normality of the data was validated using

702 the Kolmogorov-Smirnov test. To evaluate the effects of knocking down the expression of
703 *Atp2b2* in PC12 neurons on Ca^{2+} levels in basal conditions and in response to TPC2 agonists
704 and KCl, two-tailed unpaired t tests with 95% confidence interval were performed, degree of
705 freedom (df) = 24, df = 10 and df = 14, respectively, using the Prism software (version 10.4.1).
706 The same analysis was used to evaluate the effect of knocking down *Atp2b2* on sphingosine
707 (df = 9) and GSLs levels (df =10) and to compare the gene expression in *Npc1*-null mice to
708 WT mice (df = 6).
709

Acknowledgement and funding

This research has received funding from the Aligning Science Across Parkinson's [ASAP-000478 (M.E.F.S., J.W.B., D.T.V., J.H., M.R. and F.P.)] through the Michael J. Fox Foundation for Parkinson's Research (MJFF) and the Dolby Foundation (J.H.). Additional funding was provided by NPSuisse, the Australian NPC Disease Foundation (ANPDF), Niemann-Pick UK (NPUK), and the Niemann-Pick Research Fund (NPRF). M.E.F.S held a Royal Society Newton International Fellow (ref NF171121). F.M.P. is a Royal Society Wolfson Research Merit Award holder.

Biorender: Figure 3 and Supplementary Figure 4 were completely or partially created using Biorender.

Author Contributions:

M.E.F.S., R.B., J.W.B., G.P., M.G.P., R.R., D.T.V., D.S., Y.W., E.A.F., L. P., L.S.P., A.M., and L.D.: Acquisition and analysis of data. M.E.F.S., R.B., M.R. and F.P.: Drafting of the manuscript. M.E.F.S. and F.P.: Conception and design of the study. D.G.C., E.E., D.A., C.P.P., A.G., S.N., J.H., S.P. and M.R. supervised experiments, provided resources and contributed to methodology. F.M.P. supervised the entire study.

Data Availability

All data supporting the findings of this study are within the paper or available from the open repository Zenodo with the identifier DOI:10.5281/zenodo.17209111.

Code availability

Code generated on this study for HPLC data analysis (HPLC-RS) is available from: https://github.com/ArchercatNEO/HPLC/tree/v0.9

Code used to analyse transcriptomic data is available from: https://github.com/Jbrenton191/RNAseq_splicing_pipeline.

Conflict of interests

There are no conflicts of interest relevant to the data in this manuscript declared by any of the authors.

743 **References**

744 1 Strehler, E. E. Plasma membrane calcium ATPases: From generic Ca(2+) sump pumps
745 to versatile systems for fine-tuning cellular Ca(2.). *Biochem Biophys Res Commun* **460**,
746 26-33 (2015). https://doi.org:10.1016/j.bbrc.2015.01.121
747 2 Vicario, M. *et al.* A V1143F mutation in the neuronal-enriched isoform 2 of the PMCA
748 pump is linked with ataxia. *Neurobiol Dis* **115**, 157-166 (2018).
749 https://doi.org:10.1016/j.nbd.2018.04.009
750 3 Kurnellas, M. P. *et al.* Molecular alterations in the cerebellum of the plasma membrane
751 calcium ATPase 2 (PMCA2)-null mouse indicate abnormalities in Purkinje neurons.
752 *Mol Cell Neurosci* **34**, 178-188 (2007). https://doi.org:10.1016/j.mcn.2006.10.010
753 4 Vallese, F. *et al.* The ataxia-linked E1081Q mutation affects the sub-plasma membrane
754 Ca(2+)-microdomains by tuning PMCA3 activity. *Cell Death Dis* **13**, 855 (2022).
755 https://doi.org:10.1038/s41419-022-05300-y
756 5 Brendel, A., Renziehausen, J., Behl, C. & Hajieva, P. Downregulation of PMCA2
757 increases the vulnerability of midbrain neurons to mitochondrial complex I inhibition.
758 *Neurotoxicology* **40**, 43-51 (2014). https://doi.org:10.1016/j.neuro.2013.11.003
759 6 Kowalski, A. *et al.* Monomeric alpha-synuclein activates the plasma membrane
760 calcium pump. *EMBO J* **42**, e111122 (2023).
761 https://doi.org:10.15252/embj.2022111122
762 7 Colaco, A. *et al.* Unbiased yeast screens identify cellular pathways affected in
763 Niemann-Pick disease type C. *Life Sci Alliance* **3** (2020).
764 https://doi.org:10.26508/lsa.201800253
765 8 Lloyd-Evans, E. *et al.* Niemann-Pick disease type C1 is a sphingosine storage disease
766 that causes deregulation of lysosomal calcium. *Nat Med* **14**, 1247-1255 (2008).
767 https://doi.org:10.1038/nm.1876
768 9 Kilpatrick, B. S. *et al.* Endoplasmic reticulum and lysosomal Ca(2)(+) stores are
769 remodelled in GBA1-linked Parkinson disease patient fibroblasts. *Cell Calcium* **59**, 12-
770 20 (2016). https://doi.org:10.1016/j.ceca.2015.11.002
771 10 Wiatrak, B., Kubis-Kubiak, A., Piwowar, A. & Barg, E. PC12 Cell Line: Cell Types,
772 Coating of Culture Vessels, Differentiation and Other Culture Conditions. *Cells* **9**
773 (2020). https://doi.org:10.3390/cells9040958
774 11 Boczek, T. *et al.* Plasma membrane Ca2+-ATPase isoforms composition regulates
775 cellular pH homeostasis in differentiating PC12 cells in a manner dependent on
776 cytosolic Ca2+ elevations. *PLoS One* **9**, e102352 (2014).
777 https://doi.org:10.1371/journal.pone.0102352
778 12 Saarela, D. *et al.* Tagless LysoIP for immunoaffinity enrichment of native lysosomes
779 from clinical samples. *J Clin Invest* **135** (2024). https://doi.org:10.1172/JCI183592
780 13 Gerndt, S. *et al.* Agonist-mediated switching of ion selectivity in TPC2 differentially
781 promotes lysosomal function. *Elife* **9** (2020). https://doi.org:10.7554/eLife.54712
782 14 Staudt, C., Puissant, E. & Boonen, M. Subcellular Trafficking of Mammalian
783 Lysosomal Proteins: An Extended View. *Int J Mol Sci* **18** (2016).
784 https://doi.org:10.3390/ijms18010047
785 15 Palmieri, M. *et al.* Characterization of the CLEAR network reveals an integrated
786 control of cellular clearance pathways. *Hum Mol Genet* **20**, 3852-3866 (2011).
787 https://doi.org:10.1093/hmg/ddr306
788 16 Cunningham, K. W. & Fink, G. R. Calcineurin-dependent growth control in
789 Saccharomyces cerevisiae mutants lacking PMC1, a homolog of plasma membrane
790 Ca2+ ATPases. *J Cell Biol* **124**, 351-363 (1994). https://doi.org:10.1083/jcb.124.3.351

17 Moniakis, J., Coukell, M. B. & Janiec, A. Involvement of the Ca2+-ATPase PAT1 and the contractile vacuole in calcium regulation in Dictyostelium discoideum. *J Cell Sci* **112 (Pt 3)**, 405-414 (1999). https://doi.org:10.1242/jcs.112.3.405

18 Robak, L. A. *et al.* Excessive burden of lysosomal storage disorder gene variants in Parkinson's disease. *Brain* **140**, 3191-3203 (2017). https://doi.org:10.1093/brain/awx285

19 Feleke, R. *et al.* Cross-platform transcriptional profiling identifies common and distinct molecular pathologies in Lewy body diseases. *Acta Neuropathol* **142**, 449-474 (2021). https://doi.org:10.1007/s00401-021-02343-x

20 Hoglinger, D. *et al.* NPC1 regulates ER contacts with endocytic organelles to mediate cholesterol egress. *Nat Commun* **10**, 4276 (2019). https://doi.org:10.1038/s41467-019-12152-2

21 Peake, K. B. & Vance, J. E. Defective cholesterol trafficking in Niemann-Pick C-deficient cells. *FEBS Lett* **584**, 2731-2739 (2010). https://doi.org:10.1016/j.febslet.2010.04.047

22 van den Boomen, D. J. H. *et al.* A trimeric Rab7 GEF controls NPC1-dependent lysosomal cholesterol export. *Nat Commun* **11**, 5559 (2020). https://doi.org:10.1038/s41467-020-19032-0

23 Morgan, A. J., Davis, L. C. & Galione, A. Choreographing endo-lysosomal Ca(2+) throughout the life of a phagosome. *Biochim Biophys Acta Mol Cell Res* **1868**, 119040 (2021). https://doi.org:10.1016/j.bbamcr.2021.119040

24 Feng, X. & Yang, J. Lysosomal Calcium in Neurodegeneration. *Messenger (Los Angel)* **5**, 56-66 (2016). https://doi.org:10.1166/msr.2016.1055

25 Chen, R. *et al.* TMEM165 replenishes lysosomal Ca²⁺ stores, protects cells against Ca²⁺ overload, and mediates Ca²⁺-induced lysosomal H⁺ leakage. *bioRxiv*, 2024.2005.2009.593345 (2024). https://doi.org:10.1101/2024.05.09.593345

26 Zajac, M. *et al.* A mechanism of lysosomal calcium entry. *Sci Adv* **10**, eadk2317 (2024). https://doi.org:10.1126/sciadv.adk2317

27 Morgan, A. J., Platt, F. M., Lloyd-Evans, E. & Galione, A. Molecular mechanisms of endolysosomal Ca2+ signalling in health and disease. *Biochem J* **439**, 349-374 (2011). https://doi.org:10.1042/BJ20110949

28 Kim, S. *et al.* Disruptive lysosomal-metabolic signaling and neurodevelopmental deficits that precede Purkinje cell loss in a mouse model of Niemann-Pick Type-C disease. *Sci Rep* **13**, 5665 (2023). https://doi.org:10.1038/s41598-023-32971-0

29 Huebecker, M. *et al.* Reduced sphingolipid hydrolase activities, substrate accumulation and ganglioside decline in Parkinson's disease. *Mol Neurodegener* **14**, 40 (2019). https://doi.org:10.1186/s13024-019-0339-z

30 Te Vruchte, D. *et al.* Glycosphingolipid Changes in Plasma in Parkinson's Disease Independent of Glucosylceramide Levels. *Mov Disord* **37**, 2129-2134 (2022). https://doi.org:10.1002/mds.29163

31 Calvo, D., Gomez-Coronado, D., Suarez, Y., Lasuncion, M. A. & Vega, M. A. Human CD36 is a high affinity receptor for the native lipoproteins HDL, LDL, and VLDL. *J Lipid Res* **39**, 777-788 (1998).

32 Bolte, S. & Cordelieres, F. P. A guided tour into subcellular colocalization analysis in light microscopy. *J Microsc* **224**, 213-232 (2006). https://doi.org:10.1111/j.1365-2818.2006.01706.x

33 Neville, D. C. *et al.* Analysis of fluorescently labeled glycosphingolipid-derived oligosaccharides following ceramide glycanase digestion and anthranilic acid labeling. *Anal Biochem* **331**, 275-282 (2004). https://doi.org:10.1016/j.ab.2004.03.051

34 Priestman, D. A., Weng, Y., Sabir, M., Bush, R., Wallom, K., Fernández-Suárez, M.E., Platt, F.M., te Vruchte, D. Analysis of glycosphingolipids from cell lines. *protocols.io* (2024). https://doi.org:https://dx.doi.org/10.17504/protocols.io.x54v9pn14g3e/v1

35 Danielle te Vruchte, Y. W., Mylene Huebecker, Kerri-Lee Wallom, Frances M Platt. Analysis of sphingosine, sphinganine and glucosylsphingosine from cells, animal tissues and plasma. *protocols.io* (2025). https://doi.org:dx.doi.org/10.17504/protocols.io.bp2l6zkz1gqe/v1

36 Di Tommaso, P. *et al.* Nextflow enables reproducible computational workflows. *Nat Biotechnol* **35**, 316-319 (2017). https://doi.org:10.1038/nbt.3820

37 Frankish, A. *et al.* GENCODE: reference annotation for the human and mouse genomes in 2023. *Nucleic Acids Res* **51**, D942-D949 (2023). https://doi.org:10.1093/nar/gkac1071

38 Chen, S., Zhou, Y., Chen, Y. & Gu, J. fastp: an ultra-fast all-in-one FASTQ preprocessor. *Bioinformatics* **34**, i884-i890 (2018). https://doi.org:10.1093/bioinformatics/bty560

39 Patro, R., Duggal, G., Love, M. I., Irizarry, R. A. & Kingsford, C. Salmon provides fast and bias-aware quantification of transcript expression. *Nat Methods* **14**, 417-419 (2017). https://doi.org:10.1038/nmeth.4197

40 Andrews, S. FastQC: A Quality Control tool for High Throughput Sequence Data. *Babraham Bioinformatics* (2010).

41 Wang, L., Wang, S. & Li, W. RSeQC: quality control of RNA-seq experiments. *Bioinformatics* **28**, 2184-2185 (2012). https://doi.org:10.1093/bioinformatics/bts356

42 Okonechnikov, K., Conesa, A. & Garcia-Alcalde, F. Qualimap 2: advanced multi-sample quality control for high-throughput sequencing data. *Bioinformatics* **32**, 292-294 (2016). https://doi.org:10.1093/bioinformatics/btv566

43 Picard. Picard2019toolkit. *Broad Institute* **v2.27.5** (2019).

44 Ewels, P., Magnusson, M., Lundin, S. & Kaller, M. MultiQC: summarize analysis results for multiple tools and samples in a single report. *Bioinformatics* **32**, 3047-3048 (2016). https://doi.org:10.1093/bioinformatics/btw354

45 Brenton, J. RNAseq_splicing_pipeline: Human RNAseq Alignment and QC for Differential Expression and Splicing Analysis. *Zenodo* (2024). https://doi.org:doi:10.5281/zenodo.13379191.

46 Li, Y. I. *et al.* Annotation-free quantification of RNA splicing using LeafCutter. *Nat Genet* **50**, 151-158 (2018). https://doi.org:10.1038/s41588-017-0004-9

47 Perez, G. *et al.* The UCSC Genome Browser database: 2025 update. *Nucleic Acids Res* **53**, D1243-D1249 (2025). https://doi.org:10.1093/nar/gkae974

48 Abramson, J. *et al.* Accurate structure prediction of biomolecular interactions with AlphaFold 3. *Nature* **630**, 493-500 (2024). https://doi.org:10.1038/s41586-024-07487-w